Chemical Engineering Journal 464 (2023) 142711

Contents lists available at ScienceDirect

Chemical Engineering Journal

journal homepage: www.elsevier.com/locate/cej

Engineering d-p orbital hybridization through regulation of interband energy separation for durable aqueous Zn//VO_2(B) batteries

Wenwei Zhang [a,1], Jianfeng Liu [b,1], Wanyue Cai [c], Min Zhou [b], Wenhui Zhong [c], Gaofan Xiao [b], Ping Luo [c,*], Yan Zhao [d,*], Qinyou An [a,e,*]

[a] State Key Laboratory of Advanced Technology for Materials Synthesis and Processing, Wuhan University of Technology, Wuhan 430070, China
[b] State Key Laboratory of Silicate Materials for Architectures, International School of Materials Science and Engineering, Wuhan University of Technology, 430070, China
[c] Hubei Provincial Key Laboratory of Green Materials for Light Industry, Hubei Engineering Laboratory of Automotive Lightweight Materials and Processing, New Materials and Green Manufacturing Talent Introduction and Innovation Demonstration Base School of Materials and Chemical Engineering, Hubei University of Technology, Wuhan 430068, China
[d] College of Materials Science and Engineering, Sichuan University, Chengdu 610065, China
[e] Hubei Longzhong Laboratory, Wuhan University of Technology, Xiangyang Demonstration Zone, Xiangyang, Hubei 441000, China

ARTICLE INFO

Keywords:
Aqueous zinc-ion battery
Electronic structure
VO_2(B)
Heteroatomic doping
Energy difference

ABSTRACT

VO_2(B) is considered as the leading candidate cathode materials for AZIBs, however, the primary challenge of slow kinetics and limited actual capacity remains unresolved to date well in modification strategy. Significantly, the insights into the mechanism of ion doping, one of the most effective measures, have not been explored well. Herein, we proposed and unveil that reactivity of vanadium atoms and the Zn^{2+} ion adsorption energy in VO_2(B) can be related to the theoretical model Δd-p based on the band-center of heteroatom and surrounding coordination oxygen via the density functional theory (DFT). Accordingly, the heteroatom (Cr, Mo and W)-doped VO_2(B) cathode was proposed for AZIBs and it can well verify the above theoretical calculation results. Typically, the Mo-doped VO_2(B) delivers the best comprehensive electrochemical performance, and it owns excellent initial specific capacity (264.6 mA h g^{-1}) and retention rate (81.4 %) can be obtained at the 3.0 A g^{-1} after 3000 cycles. And, it also shows a much faster Zn^{2+} ion diffusion coefficient (2.1×10^{-8} *vs* 2.6×10^{-9} cm^2 S^{-1}) than that of pure VO_2(B). Meanwhile, the promising energy density of 207.3 Wh kg^{-1} at 0.1 A g^{-1} and power density of 3094.5 W kg^{-1} at 5.0 A g^{-1} also was achieved. This finding can help understand the modification mechanism of heteroatom-doping materials and fundamentally guide the electrode design to improve performance.

1. Introduction

Recently, compared with monovalent metal ions, polyvalent ion batteries have been widely developed due to the excess of one electron transfer [1–7]. Notably, aqueous zinc ion batteries (AZIBs) have received more attention due to the advantages of water-based electrolyte and metal zinc with abundant resources, which can help obtain faster ion migration rate, higher security, environmental friendliness and reduced cost, etc [8–14]. However, due to the strong electrostatic interaction between highly polar Zn^{2+} ions and host materials, the low conductivity of inorganic compounds has become a factor that hinders the further development of zinc ion batteries. Thus, exploring efficient cathode materials which possess stable structure, excellent electrical conductivity and cycle performance is crucial for aqueous zinc ion batteries (AZIBs) in the field of grid-scale energy storage [11,15–18].

Among the proposed cathode materials system, VO_2(B), as common vanadium-based material with a stable tunnel structure, varied valence states of vanadium and other advantages, has been used to store charge ions (e.g. Alkali metal ions, polyvalent metal ions, etc.) [19–21]. However, the ability and development of VO_2(B) to store Zn^{2+} ions were greatly hindered by the limited actual capacity and sluggish ion/electron transport dynamics. Interestingly, the existing issues can be eased

* Corresponding authors at: State Key Laboratory of Advanced Technology for Materials Synthesis and Processing, Wuhan University of Technology, Wuhan 430070, China (Q. An).
E-mail addresses: blueknight_0930@163.com (P. Luo), yanzhao@scu.edu.cn (Y. Zhao), anqinyou86@whut.edu.cn (Q. An).
[1] W. Zhang and J. Liu contributed equally to this work.

https://doi.org/10.1016/j.cej.2023.142711
Received 16 November 2022; Received in revised form 13 March 2023; Accepted 29 March 2023

well through proposed strategies such as adjusting bulk crystal structure [22–25], special morphology structure engineering [26,27], and combining with conductive materials [20,21,28,29], etc. Especially, the heteroatoms doping engineering is often regarded as one of the most effective, basic and widespread modification methods based on the fundamentally rearranged atomic distribution and electronic structure. Transition metal elements (TMEs) doping have selected as a modified regulator, benefiting from the special physical/chemical properties and d orbital electronic. [23,30–33].

However, the issue of the modification mechanism of transition metal doping has not been fully studied and proved well in AZIBs. Usually, the TMEs with different energy level will significantly affect the framework properties by orbital interactions with the p orbital of nonmetallic atoms (eg. O and S atom.) after introducing the TMEs into host-material. Meanwhile, most of the common published research work lacks the corresponding element screening mechanism due to single element doping way and inapplicable d-band-center theories or other intrinsic descriptors. Ni^{2+}, W^{6+} and Mn^{2+} ion, etc. has been singly introduced into VO_2(B) for improved performance, but the mechanism of atomic doping modification was not explained well [23,34,35].

Therefore, the above discussion not only indicates that the defects in Zn^{2+} ion storage of VO_2(B) need to be reasonable and relatively fundamental solution, but also highlights the significance and necessity of dopant selection on the different n-d TMEs and simultaneously understand the modification mechanism when used as doping modification.

Herein, Δd-p has been proposed as a descriptor for the selection of suitable heteroatoms based on the results of Density Functional Theory (DFT) calculations. Subsequently, the VI B group element (Cr, Mo and W) doped VO_2(B) material (noted as CVO, MVO and WVO) was prepared as cathode for AZIBs to verify the above theoretical calculation results, which can be found that the experimental results are in good agreement with the theoretical calculation results. Finally, the Zn^{2+} ion storage mechanism of selected MVO also was investigated by various in/ex-situ characterization techniques. This paper presented descriptor, Δd-p between dopant and oxygen atom, which may provide considerable mode to screen dopants for aqueous zinc-ion batteries (AZIBs) and other metal-ion batteries.

2. Experimental section

2.1. Synthesis of materials

All chemicals are used directly after purchase without any pretreatment. $Cr(NO_3)_3{\cdot}9H_2O$ (Macklin, 99.99%). $(NH_4)_6Mo_7O_{24}{\cdot}4H_2O$ (Macklin, 99.9% metals basis). $(NH_4)_{10}H_2(W_2O_7)_6{\cdot}xH_2O$ (Macklin, 99.95% metals basis). $C_2H_2O_4{\cdot}2H_2O$: (Macklin, AR, ≥99.5%). V_2O_5 (Macklin, AR, ≥99.5%).

The purity of the chemicals produced by manufacturer Macklin has met the requirements of this research.

Doped—VO_2(B): Firstly, 4 mmol $C_2H_2O_4{\cdot}2H_2O$ and an amount of heteroatoms source ($Cr(NO_3)_3{\cdot}9H_2O$, $(NH_4)_6Mo_7O_{24}{\cdot}4H_2O$ and $(NH_4)_{10}H_2(W_2O_7)_6{\cdot}xH_2O$) was dissolved in 40 ml deionized water and stirred magnetically at room temperature; secondly, 2 mmol V_2O_5 were added to the above solution and magnetic stirring continued for 3 h; thirdly, the above solution was transferred into 50 ml Teflon-lined autoclave and heated at 180 ℃ for 24 h. Finally, the sample was dried at 60℃ for 12 h after it was washed with deionized water and alcohol several times.

Pure–VO_2: It was synthesized as the above similar process without adding $Cr(NO_3)_3{\cdot}9H_2O$, $(NH_4)_6Mo_7O_{24}{\cdot}4H_2O$ and $(NH_4)_{10}H_2(W_2O_7)_6{\cdot}xH_2O$.

2.2. Materials characterization

The crystallographic characterization of the cathode materials (CVO, MVO, WVO and PVO) was measured by a Bruker D8 Discover XRD with Cu Kα radiation (λ = 1.5418 Å). SEM images were collected by a JEOL-7100F microscope with an acceleration voltage of 20 kV. TEM, energy dispersive X-ray spectroscopy (EDX) element mapping, and high-resolution transmission electron microscopy (HRTEM) images were recorded using a Titan G2 60–300 transmission electron microscope. Raman spectrum measurement was implemented by a Renishaw RM-1000 laser Raman microscopy system. X-ray photoelectron spectroscope (XPS) measurement was achieved by using the VG K-Alpha Probe spectrometer (Thermofisher Scientific) with Al Ka radiation as the excitation source. Raman (Renishaw INVIA) was applied to obtain the spectra and ex-situ Raman spectra of the cathode material.

These experimental instruments have been in our laboratory, which can not only meet the material characterization analysis required by this research, but also save time and cost.

2.3. The preparation of electrode and electrochemical measurements

Firstly, the active material (CVO, MVO, WVO and PVO), conductive agent (acetylene black) and binder (PVDF) are added to a mortar to mix evenly according to the weight ratio of 7:2:1; then the slurry is uniform Coated on the titanium foil; finally, it was placed in a vacuum drying oven for drying at 70 °C. The mass loading of the cathode keeps the average 1.5 mg cm^{-2}.

Subsequently, the CR 2016-type coin cells were assembled in the air using 3 M $Zn(CF_3SO_3)_2$ (TCI, >99.0%(T)) solution, metal zinc foil and glass fiber membranes as electrolyte, anode and separator, respectively. Then, LAND battery testing system (CT2001A, Wuhan, China) within the potential windows of 0.2–1.4 V was used to evaluate the electrochemical performances and Zn^{2+} ion diffusion coefficient; While the cyclic voltammetry (CV) and electrochemical impedance spectroscopy (EIS) measurements were tested by an electrochemical workstation (CHI760E and Autolab PGSTAT 302 N) at room temperature.

The LAND battery testing system and electrochemical workstation with high sensitivity and accuracy have been in our laboratory, which can help us obtain the required electrochemical performance data in this research.

2.4. Density functional theory calculations

Constructing the Cr, Mo and W atom inserted VO_2(B) model by replacing a V atom with a dopant atom and used as an example to qualitatively illuminate the effect of heteroatom on the electronic structure of VO_2(B).

All density functional theory (DFT) calculations were carried out Vienna ab initio Simulation package (VASP) [36]. The plane-wave cutoff energy was 500 eV. The convergence of energy and forces were set to 1×10^{-5} eV and 0.02 eV/Å, respectively. 3×4×3 k-points were used to sample the Brillouin zone. The Grimme's dispersion correction method for DFT-D3 is used to account for the van der Waals (vdW) interactions2 [37]. Then Climbing Image-Nudged elastic band (CI-NEB) calculations were performed to determine the activation barrier of Zn ion diffusion in the optimized structure [38]. Crystal structure diagrams were drawn with Visualization for Electronical and Structural Analysis (VESTA) [39].

Compared with other computing platforms, VASP has the advantages of faster computing speed, more accurate results and convenient operation. And the calculation parameters (such as plane-wave cutoff energy, convergence of energy and forces, etc.) can also meet the requirements of the results in this paper. The van der Waals (vdW) interactions can be well handled by DFT-D3. CI-NEB has high accuracy and universality in dealing with transition state problems. VESTA has good operation to visualize the crystal structure.

2.5. Calculation formula

In this paper, the formation energy (E_f) can usually be calculated by the following formulation.

$$E_{f-Sub.} = (E_{doped-VO2} + E_{single-V} - E_{\text{single-Cr}} - E_{\text{VO2}}) \quad (1)$$

$$E_{f-Int.} = (E_{doped-VO2} - E_{\text{single-Cr}} - E_{\text{VO2}}) \quad (2)$$

Where the $E_{doped-VO2}$ and E_{VO2} represent the total energy of doped-VO_2 and pure-VO_2, respectively. And $E_{single-V}$ and $E_{\text{single-Cr}}$ are the energy of the single metal atom.

The adsorption energy (E_{ads}) of the Zn atom is defined by the following equation

$$E_{ads} = E_{Zn@doped-VO2/PVO} - E_{doped-VO2/PVO} - E_{Zn} \quad (3)$$

Where E_{Zn} is the cohesive energy in the metal Zn and $E_{Zn@doped-VO2/PVO}$ and $E_{doped-VO2/PVO}$ are the total energies of doped-VO_2/pure VO_2 with and without Zn^{2+} ion adsorption, respectively.

The diffusion coefficient of the Zn^{2+} ion in the electrode is mainly calculated according to the following formula:

$$D_{Zn^{2+}} = \frac{4}{\pi\tau}\left(\frac{m_B V_M}{M_B S}\right)^2 \left(\frac{\Delta Es}{\Delta Et}\right)^2 \quad (4)$$

where D_{Zn}^{2+} ($cm^2\ s^{-1}$) is the diffusion coefficient of Zn^{2+}; τ (s) is the current pulse time, m_B (g) is the amount of active material in the electrode, V_M ($cm^3\ mol^{-1}$) is the molar volume of the active material, M_B (g mol^{-1}) is the molecular weight of the active material, S (cm^2) is the geometric contact area of the electrode with the electrolyte, ΔEs (V) is the potential change between two consecutive relaxation steps, ΔEt (V) is the potential change during the constant current pulse

3. Results and discussions

In order to evaluate the structural stability and feasibility of the experimental synthesis, the formation energies of different heteroatoms are calculated and shown in Fig. S1. When introducing the Cr, Mo and W heteroatoms into VO_2(B) with interstitial and substitution doping way, it can be seen that there are lower formation energy of latter than former calculated by Eq. 1–2, indicating that the dominant substitution doping mode will take precedence and produce more stable structure. Thus, the subsequent calculation models are mainly based on structures derived from element substitution.

Then, the electron structure was investigated through density of states (DOS), which will give more intuitive information about the changes in the electronic structure. As the result shown in Fig. 1a, the PVO exhibits composite semiconductor properties with a distinct band gap (0.885 eV), while the introduction of heteroatoms causes the valence bands to shift, leading to the band gap reduction. Compared to the band gap of CVO (0.1 eV) and WVO (0.565 eV), the electrons of MVO fill the conduction band thus the energy band across the Fermi level exhibiting the evident metal properties. Additionally, the energy band is calculated and supplemented to further prove and discuss the conductivity and electronic structure of P/C/M/WVO, as shown in the Fig. S2. The band gap of P/C/M/WVO is consistent with the previously calculated band gap, and the MVO still exhibits the most competitive conductivity. To further analyze the change of electronic structure, the Project density of States (PDOS) of Vanadium and Oxygen atoms are calculated and shown in Fig. 1b and c. The results shows that the reduction of the band gap in MVO is due to the Vanadium and Oxygen atoms being influenced by the heterogeneous atoms, which leads to the formation of bonding orbitals near the Fermi level, resulting in the enhancement of the activity of Vanadium and Oxygen atoms. A previous study has demonstrated that the surface reactivity of electrode materials can be optimized by the enhanced electronic conductivity[34].

Subsequently, the PDOS of heteroatoms and surrounding oxygen atoms were further investigated and calculated to find out the intrinsic mechanism of electronic structure interaction between metals and non-metal atoms. Usually, the electron will transfer from the p-orbital of oxygen to the empty d-orbital of the metal atom during the process of forming chemical bonds. The energy difference of d-p orbitals will significantly determine the electronic promotion energy for the chemical bond, which will obviously impact the constituent atomic properties and corresponding chemical bond. In general, there is a more significant effect on the other atoms based on the much more varied Δd-p than the

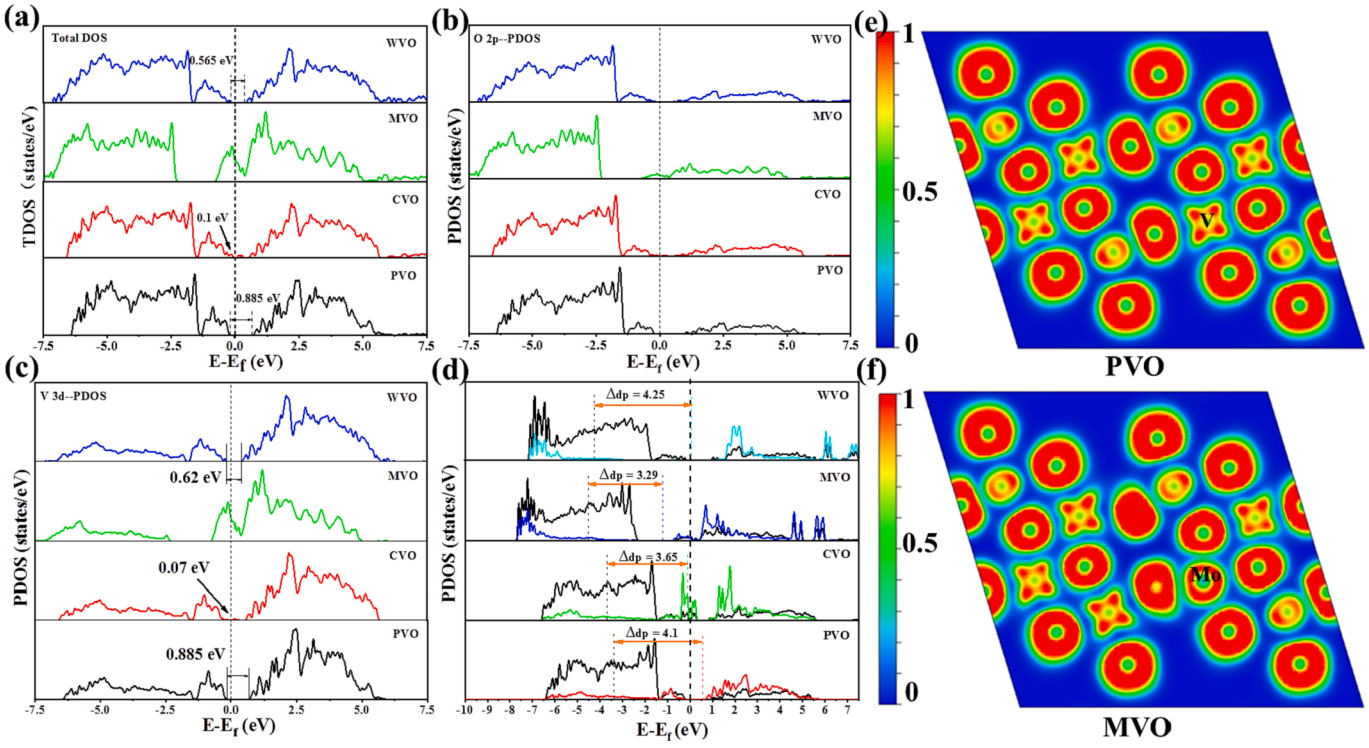

Fig. 1. (a) Total DOS, (b) PDOS of oxygen atom and (c) vanadium atom in P-, C-, M- and WVO, respectively. (d) PDOS and Δd-p for PVO, CVO, MVO and WVO, respectively. (e-f) 2D electronic location function of PVO and MVO.

perfect initial structure. And recently, similar results also have been proposed and discussed to elucidate the mechanism[40,41]. As the results show that the MVO has the smaller Δd-p value of 3.26 than the CVO, WVO and PVO (3.65, 4.25 and 4.1, respectively) in Fig. 1d, indicating the strongest interaction of Mo-O bond and may induce more pronounced changes in electron structure. Further, it can be proved that the uniform distribution of electron structure in PVO is changed through the Mo-atom doping and there is a stronger interaction between Mo and O atoms than the initial V-O bond according to the electron local function diagram (Fig. 1e and f). In addition, this interaction significantly influences the V-O bond in the chains V-O-Mo, influencing the reactivity of vanadium atoms. Thus, tuning the electron structure by doping heteroatoms can regulate the reactivity of metal atoms at active sites in the host material.

To verify the effectiveness and rationality of the electronic structure-based descriptor of Δd-p, the Zn^{2+} ion adsorption energy in the four configurations was calculated by Eq. 3. MVO exhibits the most negative adsorption energy for Zn atoms compared to other three configurations, corresponding well with the previous electron structure analysis. Additionally, based on the adsorption structure, the charge density difference was employed to analyze for Zn^{2+} ion in modified VO_2(B) and PVO. As shown in Fig. 2b and Fig. S3, the charge density difference of PVO shows uniform distribution and the Zn atom mainly provide electrons to lead the lower valence of the V atom for the reaction process. In comparison, it can be seen that the original uniform distribution appears obvious aggregation after Zn^{2+} ion insertion due to the existence of heteroatoms. Also, this uneven charge distribution can effectively build a local electrical field to attract Zn^{2+} ions through columbic electrostatic interactions for enhanced electrical conductivity [42,43]. Moreover, it is worth noting that there are more charge fragments on oxygen and vanadium atoms in MVO than the CVO and WVO, indicating that doping of Mo atoms caused a wider range of electronic structure changes.

Furthermore, typical example can be further given that the bond lengths of the Zn-O bonds in MVO are generally shorter than that in PVO, indicating a slightly stronger interaction. Among them, the Zn-O_{29} bond length in MVO is more than its counterpart in PVO, which may be caused by the fact that the Mo-O_{29} bond length is much smaller than the value in PVO. Furthermore, the bond strength between Zn and O atoms was analyzed using crystal orbital overlap population (COHP) method. A typical example can be firstly given that the orbitals of O_{13} 2p and Zn 3d overlap each other, proving that there is indeed a chemical bond between Zn and O after Zn^{2+} insertion (Fig. 2c and d and Fig. S4). Usually, the ICOHP value can be understood as the number of bonding electrons shared between two atoms and the stronger bonding effect will be produced as the increased value. Thus, the more negative ICOHP values in MVO (-0.454) than that of PVO (-0.383), confirm the effective insertion of Zn^{2+} ion and stronger Zn-O bonds in MVO. And those above calculated dates are consistent well with the higher adsorption energy for easier Zn^{2+} ion insertion.

Overall, MVO can bind strongly with Zn atom so that it can be preferentially inserted in the host material. Significantly, the most noteworthy is that the change of adsorption energy is closely related to the Δd-p value, that is, the former will be lower gradually with the latter decreases (Fig. 2e). Thus, the Δd-p value will induce a differential effect for the doped-VO_2(B) in the Zn^{2+} ion storage process.

Finally, the Climbing Image Nudged Elastic Band (CI-NEB) method was employed to evaluate the Zn^{2+} ion diffusion kinetics difference in doped-VO_2(B) and PVO [38]. The Zn diffusion pathway profiles and energy barrier are shown in Fig. S5 and Fig. 2f, respectively. Significantly, the diffusion energy barrier of CVO, MVO and WVO is much lower than that of PVO, indicating that the formers exhibit easier Zn^{2+} diffusion process due to the changes of electron structure and thus endow faster electrochemical kinetics.

Overall, as confirmed by the above DFT calculation results and

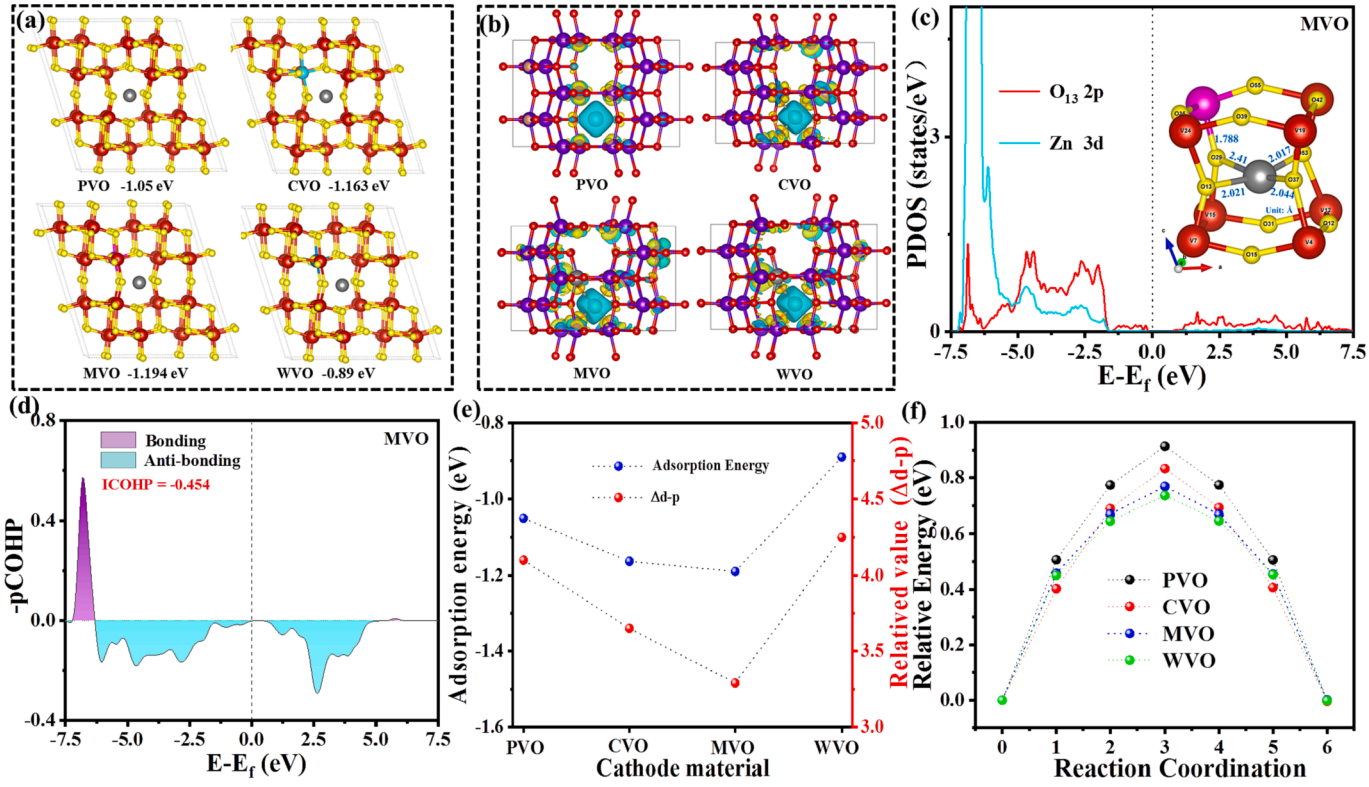

Fig. 2. (a) Adsorption structures of Zn^{2+} ion in prepared sample, and (b) the corresponding differential charge densities diagrams, the electron depletion and accumulation are drawn in cyan and yellow colors, respectively (the *iso*-surface value is 0.005 e/bohr^3). (c) Partial density of states for Zn d-orbitals and O_{13} p-orbitals, and (d) the corresponding pCOHP of the Zn–O_{13} bond. (e) Correlation between Δd-p and the Zn^{2+} ion adsorption energy. And (f) the corresponding diffusion energy barrier profiles. (For interpretation of the references to color in this figure legend, the reader is referred to the web version of this article.)

corresponding discussions, the Mo-atom can be selected as the suitable dopant for the modification according to the electronic structure-based descriptor of Δd-p among the heteroatoms.

To comprehensively demonstrate the modification mechanism of heteroatom-doping engineering for improved electrochemical performance, the cathode materials were prepared via the simple hydrothermal method in Fig. 3a under controlling heteroatoms source (Cr, Mo and W). After the hydrothermal treatment, the introduced heteroatoms will replace the vanadium atom in host materials and change the local electrical structure for higher reactivity, rapid kinetics and promoted capacity. Moreover, it can be seen from the optical photograph that the color of CVO, MVO and WVO become darker than that of PVO, which may be due to foreign ions altering the light absorption of PVO (Fig. S6). Then, the morphology/microstructure of prepared-cathode-materials was observed by SEM and TEM technology. As shown in Fig. 3b, the PVO exhibits uniform nano-belts structure, and the urchin-like CVO, MVO and nano-sheets stacked WVO are obtained after the addition of chromium/molybdenum/tungsten ions due to the change of surface energy of VO_2(B). The prepared samples all exhibit uniform element (Cr/Mo/W, V and O) distribution in Fig. S7. Furthermore, TEM results confirmed the morphology and uniform element distribution of MVO (Fig. S8).

Then, it can be observed that the XRD pattern of PVO and C-, M-, and WVO both can be consistent with the stand PDF card (Fig. 3c; 81–2392, C 2/m). And, the position of direction peaks shifted to a lower angel and the intensity also decreased at different degree due to the radius difference of foreign ions and V^{4+}, resulting in lattice distortion for different lattice constants providing larger space for facilitating the rapid transport of Zn^{2+} ions (Fig. S9).

Raman spectra with the range of 100–1200 cm^{-1} also were applied to investigate the chemical bond (Fig. 3d). And the main peaks of all samples were locking at 139, 188, 276, 403, 688 and 989 cm^{-1}, which can be attributed to monoclinic crystalline VO_2 and consistent with other literature [24,44]. The layered structure can be identified by the two peaks at 139 and 188 cm^{-1}. While the peaks located at 282 and 408 cm^{-1} belong to the V = O bending vibration bonds and the doubly

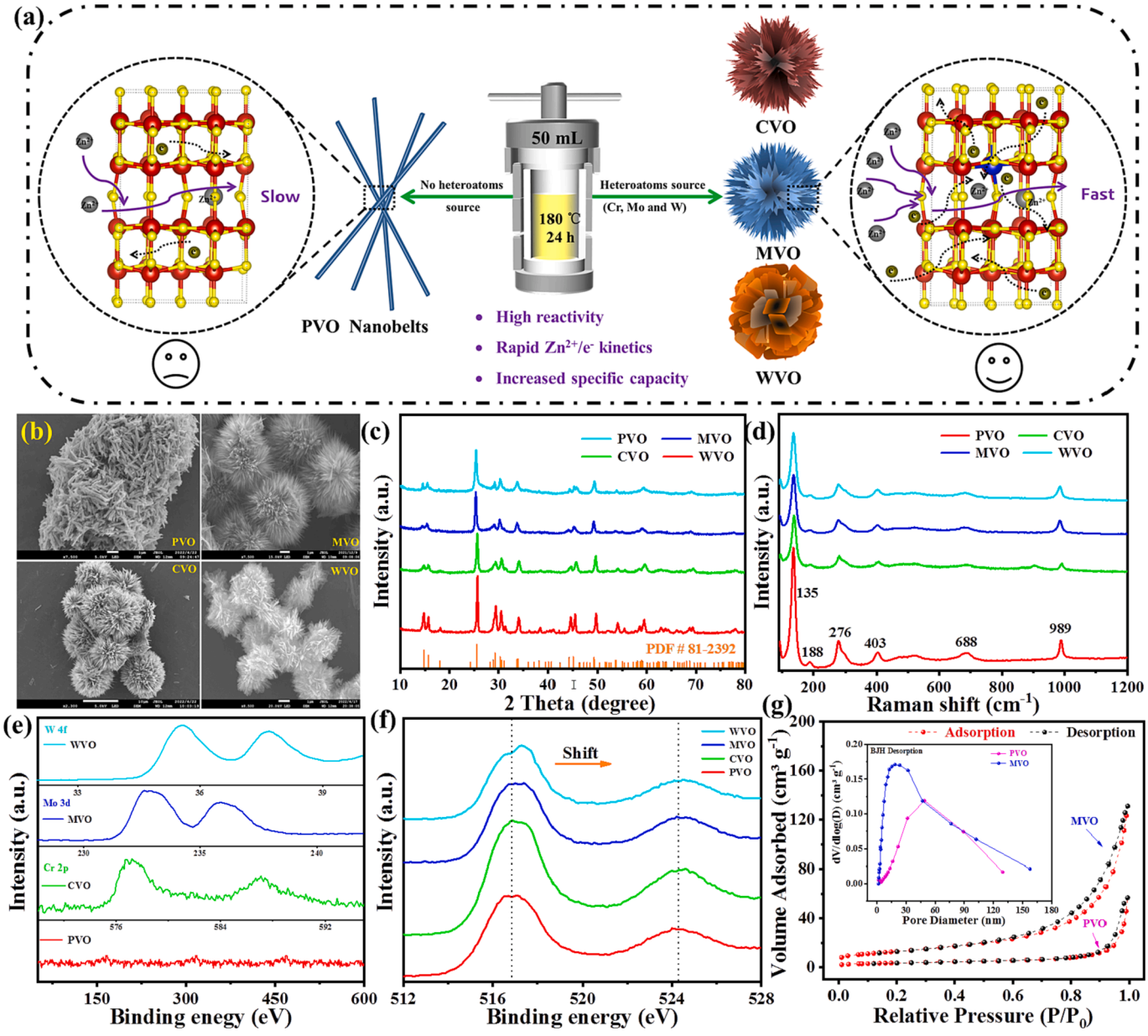

Fig. 3. (a) Synthesis process schematic of cathode materials. (b) SEM. (c) Full XRD pattern of the samples. (d) Raman. (e) High-resolution XPS spectra of doped metal ions (Cr 2p, Mo 3d and W 4f), and (f) V 2p in sample. (g) BET specific surface area and pore size distribution.

coordinated oxygen (V–O-V) stretching mode resulting from corner-shared oxygens of two pyramids can be matched with peak of 697 cm^{-1}. And, the peaks located at 989 cm^{-1} is in line with the terminal oxygen (V = O) stretching vibration [44]. However, the peak position in C-, M-, and WVO is slightly offset and its intensity is reduced, indicating the slight distortion of the crystal units. This phenomenon can be attributed to the different relative atomic masses of heteroatoms (Cr, Mo and W) and that of V as well as the different chemical bonds [45].

The XPS spectrum was further used to confirm the existence of elements and explore the valence state information of them (Fig. S10a). As shown in Fig. 3e, the orbital splitting peak of Cr 2p, Mo 3d and W 4f can confirm the existence of Cr, Mo and W elements. Moreover, it is worthy noting that the position of V 2p in C-, M-, and WVO shift to higher binding energy with a different degree, indicating that the electronic reorganization in doped-VO_2(B) due to the broken electron flow after the introduction of heteroatoms (Cr, Mo and W) in agreement with the analyses of DFT analysis (Fig. 1f). Furthermore, the V 2p energy position of MVO can be fitted as $V^{+4/+5}$, this mixed vanadium valence can lead to higher electrochemical activity and electrical conductivity (Fig. S10b) [46,47]. And, it also was further proved that Mo mainly exists in the form of +6 valence (Fig. S10c).

N_2 adsorption − desorption measurements were conducted to analyze the surface area of PVO and C-, M-, and WVO based on the significant difference in morphology structure (Fig. 3g and Table S1). It can be seen that the MVO has the biggest specific surface area and total pore volume as well as the smallest average pore diameters. Typically, the specific surface areas of MVO can reach 46.33 $m^2\ g^{-1}$ according to the Brunauer − Emmett − Teller mode while the PVO was only 12.39 $m^2\ g^{-1}$, both belonging to the type-III curves. Moreover, the pore size based on the Barrett − Joyner − Halenda plot is mainly distributed in 10 nm (15 nm *vs* PVO) and the desorption average pore diameters are about 13.5 nm (24.9 nm *vs* PVO). In conclusion, the greatly increased BET specific surface area and smaller pore diameters of MVO will provide an increased contact area between cathode and electrolyte for faster ion/electron transport kinetics and induce much enriched active sites.

The CR-2016 type AZIBs coin cells were assembled to explore the difference in storage Zn^{2+} ion ability between PVO and C-, M-, and WVO. Firstly, although the peak current of MVO is slightly smaller than that of PVO at the same scant rate of 0.1 mV s^{-1}, the area of the broad redox peak of MVO is significantly larger than that of VO_2(B), predicting the much increased specific capacity of MVO (Fig. 4a). Additionally, it is worth to note that and a new pair of higher potential redox pairs (1.05/

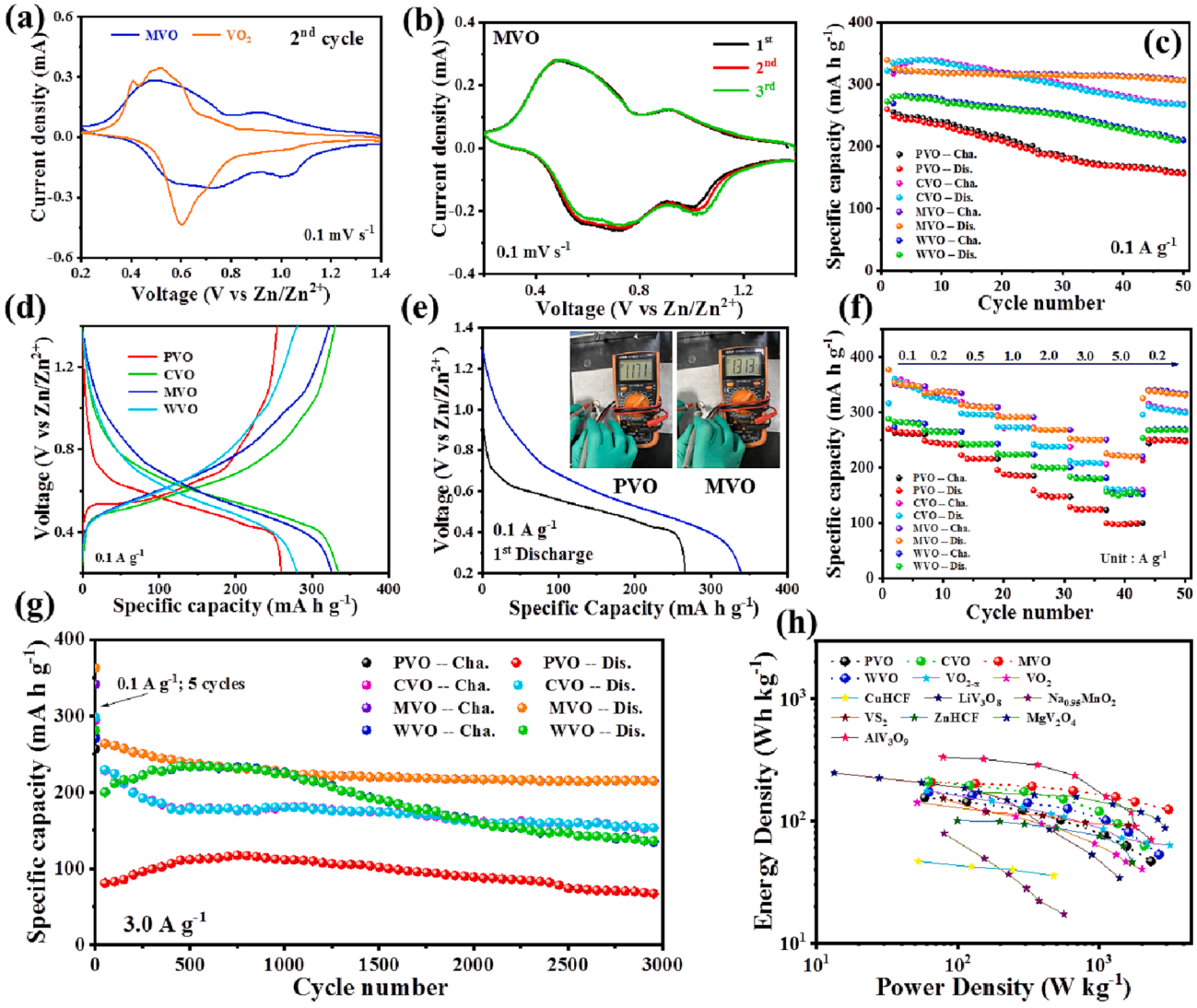

Fig. 4. (a) The comparison for typical CV curves at 0.1 mV s^{-1} between PVO//Zn and MVO//Zn battery. (b) CV curves of MVO at 0.1 mV s^{-1}. (c-d) Cycling performance and corresponding charge/discharging curves of the P-, C-, M- and WVO//Zn batteries at 0.1 A g^{-1}. (e) The discharging curves of the Zn//PVO and Zn//MVO batteries at 0.1 A g^{-1} (the insert are the open circuit voltage test). (f-g) rate performance and cycling performance 3.0 A g^{-1}. (h) The Ragone plots in comparison with other cathode materials for Zn^{2+} ion storage.

0.93 V) appears in comparison to PVO, which can be attributed to the V^{5+}/V^{4+} for achieving multi-electron reactions and the high voltage of the AZIBs [48]. Furthermore, it can be attributed to the fact that the valence electron was changed and activated after the introduction of the Mo atom. Moreover, the MVO has an almost coincident CV curve, which predicts a reversible zinc ion insertion/extraction process for excellent cyclic stability (Fig. 4b).

As a result, C-, M- and WVO all display increased specific capacity ratio of PVO at 0.1 A g^{-1}, and especially the MVO shows almost no trend of decay within the same 50 cycles (Fig. 4c), which can be consistent well with the DFT results. In addition, the Galvanostatis-Charge-Discharge (GCD) curves of C-, M-, and WVO has significantly lower over-potential and higher working voltage platform compared with PVO, which can be consistent well with the abovementioned adsorption energy and conductivity analysis (Fig. 4d). Typically, it also can be observed that the MVO//Zn batteries delivers higher open circuit voltage (V_{oc}) and much increased voltage platform (Fig. 4e). Subsequently, the rate performance of four batteries was evaluated at the various current densities (0.1, 0.2, 0.5, 1.0, 2.0, 3.0, 5.0 A g^{-1}) and the CVO, MVO, WVO/Zn batteries display much enhanced specific capacity than that of PVO. For example, the MVO//Zn batteries have a specific capacity of more than 100 mA h g^{-1} higher than the contrast sample at 5.0 A g^{-1}, indicating the excellent rate performance after the heteroatoms-doping in VO_2(B) (Fig. 4f and Fig. S11). In addition, although the CVO and WVO all have the obvious trend of capacity decline, the specific capacity is still much higher than the value of PVO at 3.0 A g^{-1} after 3000 cycles (Fig. 4g). Furthermore, the MVO//Zn battery still displays excellent cycling performance when increasing current density to 10 A g^{-1} and it also much higher than the contrast PVO//Zn battery after 12,000 cycles (Fig. S12).

In order to highlight the advance of MVO cathode, the table about the performances comparison of MVO and similar type VO_2 cathodes has been listed in Table S2. Compared to VO_2 with other modification strategy, MVO has demonstrated significantly improved comprehensive electrochemical properties. However, we also found some differences between the performance of MVO and that of other VO_2 cathode

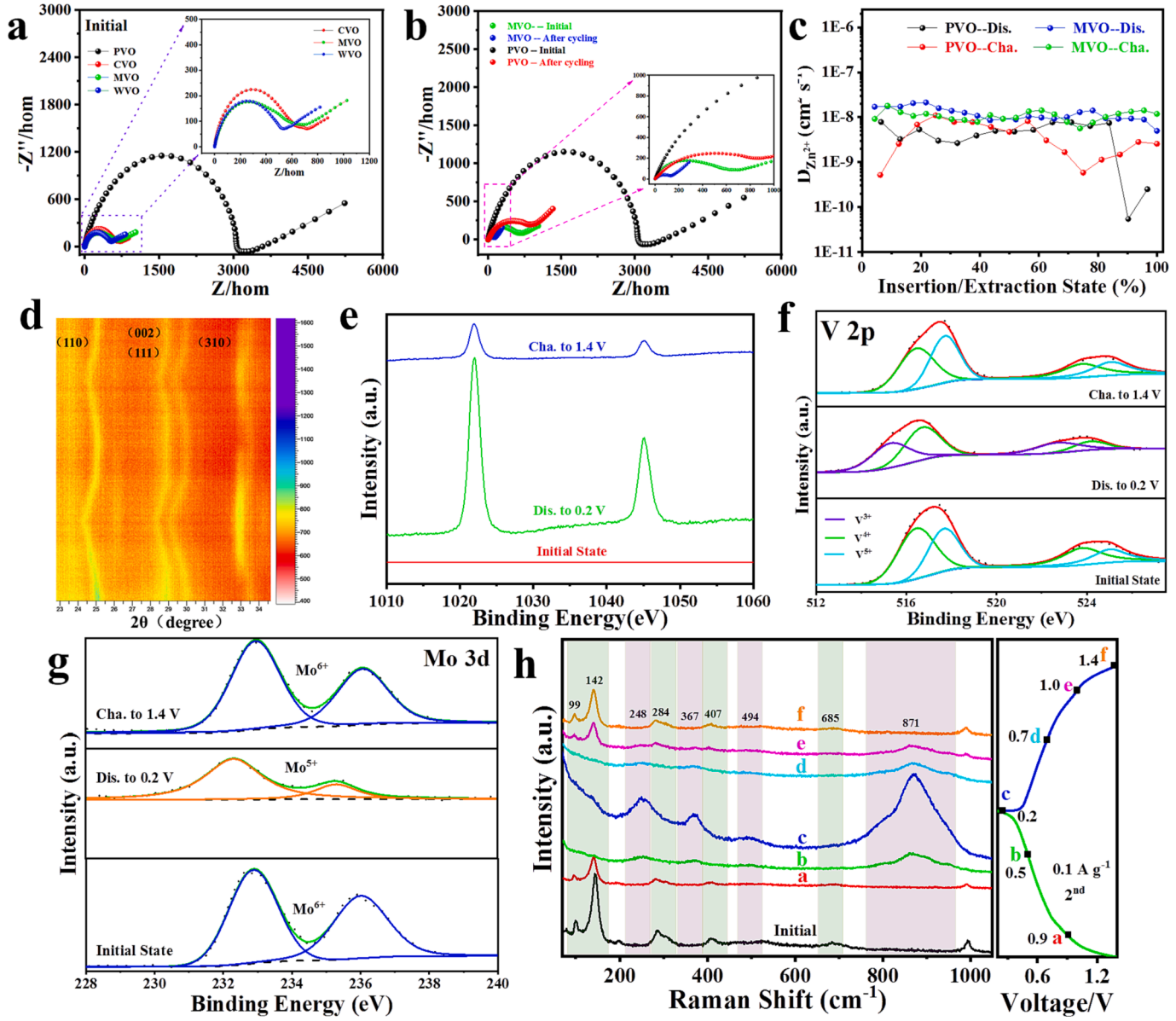

Fig. 5. (a) Nyquist diagram of four samples at initial state, and (b) the PVO and MVO before/after cycling. (c) The Zn^{2+} ion diffusion efficient in PVO and MVO electrode. (d) In-situ XRD pattern at the 1st and 2nd cycles. (e-g) Ex-situ XPS spectrum of Zn 2p, V 2p and Mo 3d at the initial, fully discharged and charged states (2nd cycle). (h) Ex-situ Raman spectrum of MVO at the second cycles.

materials (such as Ni_xVO_2 [34] and VO••-rich VO_2(B)[25], etc.), so we will further improve the comprehensive performance of VO_2 in detail in future studies.

Moreover, the power density and energy density are also necessary indicators for evaluating the advances of the proposed cathode materials. The CVO, MVO and WVO all have much improvement in energy/power density than that of PVO. Notably, it can be seen that the MVO delivers the most considerable energy density of 207.3 Wh kg^{-1} at 100 mA g^{-1} and a power density of 3094.5 W kg^{-1} at 5.0 A g^{-1}, which is great improvement over other contrast samples and existing cathode materials (Fig. 4h) [24,49–54]. However, it still needs further improvement in future studies compared to AlV_3O_9.

Furthermore, the ion/electro reaction transport kinetics process was evaluated using the electrochemical impedance spectroscopy (EIS) technology. The EIS curves of both C-, M-, WVO//Zn and PVO//Zn batteries consist of semicircles and inclined linear lines, where the diameter of the semicircle corresponds to the transfer impedance of charge at the electrode/electrolyte interface, while the slope of the straight line represents the transfer impedance of the Zn^{2+} ion inside the electrode material. Specifically, the doped-VO_2(B) exhibit significantly reduced charge transfer impedance and ion diffusion impedance in fresh electrodes according to the Fig. 5a, which can be attributed to the improvement of electrical conductivity and the favorable hierarchical morphology structure with enriched reactive sites. Furthermore, the MVO still delivers much decreased electrochemical impedance than that of PVO after electrochemical cycles (Fig. 5b). Additionally, the Zn^{2+} ion diffusion coefficient (D_{Zn2+}) calculated by Eq. (4) in MVO and PVO electrode was evaluated via the galvanostatic intermittent titration technique (GITT, Fig. S13) according to the above discussion, which shows the over-potential can be reduced after Mo-doping (Fig. S14). Specifically, the D_{Zn2+} of MVO is higher and much more stable than the value of PVO, indicating the faster and more stable Zn^{2+} transport process in MVO//Zn battery (Fig. 5c).

In a conclusion, the heteroatoms doped-VO_2(B) deliver excellent electrochemical performance than that of PVO, such as specific capacity and electrical conductivity. Among them, the Mo-doped VO_2(B) has the best overall performance, which not only proves that Mo atom is the most suitable dopant from the experimental perspective, but also indicates that the above Δd-p can be used as an effective descriptor for element screening. And this doping strategy with the adjustable band gap will help further understand the modification mechanism while maintaining similarly improved performance compared with our and others pervious published work [21,23,24,34,35,44].

In-situ XRD, ex-situ XPS and Raman spectra techniques were employed to insight the Zn^{2+} ion storage mechanism of selected MVO electrode. Firstly, the structure evolution of MVO cathode was explored at 0.1 A g^{-1} via in-situ XRD technology during the Zn^{2+} ion insertion/extraction process (1st and 2nd; Fig. 5d). The interplanar spacing of typical crystal planes (1 1 0), (0 0 2), (1 1 1) and (3 1 0) continues to expand as the Zn^{2+} ions insertion into MVO and these peaks return to their original positions when Zn^{2+} ions are released, indicating the excellent reversible Zn^{2+} ion storage process in MVO.

Then, the ex-situ XPS technology was used to identify the changes of elements in MVO during Zn^{2+} ion insertion/extraction (Fig. S15a). Firstly, the stronger zinc element signal when discharged to 0.2 V than the initial and fully Zn^{2+} ion extracted states further demonstrate that the Zn^{2+} ion can insert the MVO and come out successfully. And the weak residual zinc signal locating dead sites indicates that some Zn^{2+} ions cannot escape well, which is consistent with previous reports, but it may play a pillar effect in MVO to stabilize the structure for subsequent reversible reaction (Fig. 5e). Moreover, V^{3+} can be seen while the V^{5+} disappears and the intensity of V^{4+} is reduced, but the change can almost return back to the initial states when fully finished the charging process, indicating that the insertion/extraction of the zinc ions leads to a charge transfer of the vanadium element and excellent reversible reaction process (Fig. 5f). Additionally, it is noteworthy that Mo element also has reversible change similar to V atom in the reaction process, which proves that doped Mo can not only play a role in regulating the electron structure, but also participate in the reaction as an active atom for providing more specific capacity (Fig. 5g).

The ex-situ Raman spectrum was further applied to investigate the Zn^{2+} ion storage mechanism of MVO at the initial-two cycles. The original Raman spectrum peak gradually disappears during the continuous discharge process of the proposed battery system at the 0.1 A g^{-1}, followed by some new peaks gradually appearing at 248, 367, 494, 871 cm^{-1} and reaching the maximum intensity at the fully discharged state, which could be classified as the generated zinc vanadate compounds ($Zn_xVO_2{\cdot}nH_2O$) after zinc ion inserting (Fig. 5h). On the contrary, the stretching/vibration peaks of MVO gradually reappear and the above generated new peak disappears when the voltage increase from 0.2 to 1.4 V. And this process is similar to the first cycle (Fig. S14b), confirming the reversible intercalation/extraction reaction mechanism in MVO and consistent well with the ex-situ XRD/XPS results. As a result, the diagram of the Zn^{2+} insertion/extraction mechanism in the MVO//Zn batteries can be concluded in Fig. S16.

4. Conclusion

In conclusion, the d-p energy difference based on the band-center of heteroatom and surrounding coordination oxygen has been proposed to guide the design of metal-ion doped cathode for AZIBs. And the reactivity of vanadium atoms and the ion adsorption energy can be regulated for the promoted Zn^{2+} ion storage via DFT calculation results. Then, the comprehensive experiment results demonstrate that transition metal elements doping can substantially improve the Zn^{2+} ion storage ability of VO_2(B). Typically, the MVO performs cycle performance (81.4 % at the 3.0 A g-1 after 3000 cycles), showing much reduced electrochemical impedance and more stable Zn^{2+} diffusion coefficient (about 10^{-8} cm^2 s^{-1}). More importantly, the MVO delivers considerable energy density of 207.3 Wh kg^{-1} at 0.1 A g^{-1} and power density of 3094.5 W kg^{-1} at 5.0 A g^{-1}. Finally, the solid-solution mechanism of Zn^{2+} ion storage in MVO was demonstrated under the application of in-situ XRD, ex-situ XPS and ex-situ Raman technology. The results and relative analysis have confirmed that the theoretical model Δd-p was effective designing cathode materials for AZIBs rationally. And it also shows that understanding the modification mechanism of heteroatom-doping materials could fundamentally guide the cathode design to improve performance.

CRediT authorship contribution statement

Wenwei Zhang: Conceptualization, Methodology, Validation, Investigation, Data curation, Writing – original draft, Writing – review & editing. **Jianfeng Liu:** Conceptualization, Methodology, Validation, Investigation, Data curation, Writing – original draft, Writing – review & editing. **Wanyue Cai:** Methodology, Formal analysis. **Min Zhou:** Validation, Formal analysis. **Wenhui Zhong:** Conceptualization, Formal analysis. **Gaofan Xiao:** . **Ping Luo:** Conceptualization, Supervision. **Yan Zhao:** Conceptualization, Supervision. **Qinyou An:** Conceptualization, Supervision.

Declaration of Competing Interest

The authors declare that they have no known competing financial interests or personal relationships that could have appeared to influence the work reported in this paper.

Data availability

No data was used for the research described in the article.

Acknowledgements

This work was supported by the National Natural Science Foundation of China (52172231, 51972259), the Fundamental Research Funds for the Central Universities (WUT: 2020III043GX, 2020III015GX) and the Natural Science Foundation of Hubei Province (2022CFA087).

Appendix A. Supplementary data

Supplementary data to this article can be found online at https://doi.org/10.1016/j.cej.2023.142711.

References

[1] F. Xiong, Y. Jiang, L. Cheng, R. Yu, S. Tan, C. Tang, C. Zuo, Q. An, Y. Zhao, J.-J. Gaumet, L. Mai, Low-strain TiP_2O_7 with three-dimensional ion channels as long-life and high-rate anode material for Mg-ion batteries, Interdiscip. Mater. 1 (2022) 140–147, https://doi.org/10.1002/idm2.12004.

[2] C. Zuo, F. Xiong, J. Wang, Y. An, L. Zhang, Q. An, MnO_2 Polymorphs as Cathode Materials for Rechargeable Ca-Ion Batteries, Adv. Funct. Mater. 32 (2022) 2202975, https://doi.org/10.1002/adfm.202202975.

[3] J. Wang, J. Wang, Y. Jiang, F. Xiong, S. Tan, F. Qiao, J. Chen, Q. An, L. Mai, $CaV_6O_{16}{\cdot}2.8H_2O$ with Ca^{2+} Pillar and Water Lubrication as a High-Rate and Long-Life Cathode Material for Ca-Ion Batteries, Adv. Funct. Mater. 32 (2022) 2113030, https://doi.org/10.1002/adfm.202113030.

[4] W. Wang, Y. Jiang, Y. Yang, F. Xiong, S. Zhu, J. Wang, L. Du, J. Chen, L. Cui, J. Xie, Q. An, L. Mai, Basal Planes Unlocking and Interlayer Engineering Endows Proton Doped-$MoO_{2.8}F_{0.2}$ with Fast and Stable Magnesium Storage, ACS Nano 16 (2022) 17097–17106, https://doi.org/10.1021/acsnano.2c07399.

[5] S. Zhu, Y. Dai, J. Li, C. Ye, W. Zhou, R. Yu, X. Liao, J. Li, W. Zhang, W. Zong, R. Chen, G. He, D. Chao, Q. An, Cathodic Zn underpotential deposition: an evitable degradation mechanism in aqueous zinc-ion batteries, Sci. Bull. 67 (2022) 1882–1889, https://doi.org/10.1016/j.scib.2022.08.023.

[6] I. Kim, S. Jang, K.H. Lee, Y. Tak, G. Lee, In situ polymerized solid electrolytes for superior safety and stability of flexible solid-state Al-ion batteries, Energy Storage Mater. 40 (2021) 229–238, https://doi.org/10.1016/j.ensm.2021.05.019.

[7] R. Bagheri, M. Ghaedi, A. Asfaram, E. Alipanahpour Dil, H. Javadian, RSM-CCD design of malachite green adsorption onto activated carbon with multimodal pore size distribution prepared from Amygdalus scoparia: Kinetic and isotherm studies, Polyhedron 171 (2019) 464–472, https://doi.org/10.1016/j.poly.2019.07.037.

[8] S. Deng, Z. Yuan, Z. Tie, C. Wang, L. Song, Z. Niu, Electrochemically Induced Metal–Organic-Framework-Derived Amorphous V_2O_5 for Superior Rate Aqueous Zinc-Ion Batteries, Angew. Chem. Int. Edit. 59 (2020) 22002–22006, https://doi.org/10.1002/anie.202010287.

[9] Z. Yao, W. Zhang, X. Ren, Y. Yin, Y. Zhao, Z. Ren, Y. Sun, Q. Lei, J. Wang, L. Wang, T. Ji, P. Huai, W. Wen, X. Li, D. Zhu, R. Tai, A Volume Self-Regulation MoS_2 Superstructure Cathode for Stable and High Mass-Loaded Zn-Ion Storage, ACS Nano 16 (2022) 12095–12106, https://doi.org/10.1021/acsnano.2c02330.

[10] Z. Song, L. Miao, L. Ruhlmann, Y. Lv, D. Zhu, L. Li, L. Gan, M. Liu, Lewis Pair Interaction Self-Assembly of Carbon Superstructures Harvesting High-Energy and Ultralong-Life Zinc-Ion Storage, Adv. Funct. Mater. 32 (2022) 2208049, https://doi.org/10.1002/adfm.202208049.

[11] C. Li, S. Jin, L.A. Archer, L.F. Nazar, Toward practical aqueous zinc-ion batteries for electrochemical energy storage, Joule 6 (2022) 1733–1738, https://doi.org/10.1016/j.joule.2022.06.002.

[12] X. Wu, C. Yin, M. Zhang, Y. Xie, J. Hu, R. Long, X. Wu, X. Wu, The intercalation cathode of MOFs-driven vanadium-based composite embedded in N-doped carbon for aqueous zinc ion batteries, Chem. Eng. J. 452 (2023), 139573, https://doi.org/10.1016/j.cej.2022.139573.

[13] E. Sharifpour, E. Alipanahpour Dil, A. Asfaram, M. Ghaedi, A. Goudarzi, Optimizing adsorptive removal of malachite green and methyl orange dyes from simulated wastewater by Mn-doped CuO-Nanoparticles loaded on activated carbon using CCD-RSM: Mechanism, regeneration, isotherm, kinetic, and thermodynamic studies, Appl. Organomet. Chem. 33 (3) (2019) e4768.

[14] E. Alipanahpour Dil, M. Ghaedi, A. Asfaram, F. Mehrabi, F. Sadeghfar, Efficient adsorption of Azure B onto CNTs/Zn:ZnO@Ni_2P-NCs from aqueous solution in the presence of ultrasound wave based on multivariate optimization, J. Ind. E. Chem. 74 (2019) 55–62, https://doi.org/10.1016/j.jiec.2018.12.050.

[15] E. Alipanahpour Dil, M. Ghaedi, A. Asfaram, F. Mehrabi, A.A. Bazrafshan, L. Tayebi, Synthesis and application of Ce-doped TiO_2 nanoparticles loaded on activated carbon for ultrasound-assisted adsorption of Basic Red 46 dye, Ultrasoni. Sonochem. 58 (2019), 104702, https://doi.org/10.1016/j.ultsonch.2019.104702.

[16] E.A. Dil, M. Ghaedi, G.R. Ghezelbash, A. Asfaram, A.M. Ghaedi, F. Mehrabi, Modeling and optimization of Hg^{2+} ion biosorption by live yeast Yarrowia lipolytica 70562 from aqueous solutions under artificial neural network-genetic algorithm and response surface methodology: kinetic and equilibrium study, RSC Adv. 6 (2016) 54149–54161, https://doi.org/10.1039/C6RA11292G.

[17] Y.i. Ding, L. Zhang, X. Wang, L. Han, W. Zhang, C. Guo, Vanadium-based cathodes for aqueous zinc ion batteries: Structure, mechanism and prospects, Chinese Chem. Lett. 34 (2) (2023) 107399.

[18] X. Jia, C. Liu, Z.G. Neale, J. Yang, G. Cao, Active Materials for Aqueous Zinc Ion Batteries: Synthesis, Crystal Structure, Morphology, and Electrochemistry, Chem. Rev. 120 (2020) 7795–7866, https://doi.org/10.1021/acs.chemrev.9b00628.

[19] D. Chao, R. DeBlock, C.-H. Lai, Q. Wei, B. Dunn, H.J. Fan, Amorphous VO_2: A Pseudocapacitive Platform for High-Rate Symmetric Batteries, Adv. Mater. 33 (2021) 2103736, https://doi.org/10.1002/adma.202103736.

[20] J. Guo, L. Li, J. Luo, W. Gong, R. Pan, B. He, S. Xu, M. Liu, Y. Wang, B. Zhang, C. Wang, L. Wei, Q. Zhang, Q. Li, Polypyrrole-Assisted Nitrogen Doping Strategy to Boost Vanadium Dioxide Performance for Wearable Nonpolarity Supercapacitor and Aqueous Zinc-Ion Battery, Adv. Energy Mater. 12 (2022) 2201481, https://doi.org/10.1002/aenm.202201481.

[21] P. Luo, W. Zhang, W. Cai, Z. Huang, G. Liu, C. Liu, S. Wang, F. Chen, L. Xia, Y. Zhao, S. Dong, L. Xia, Accelerated ion/electron transport kinetics and increased active sites via local internal electric fields in heterostructured VO_2-carbon cloth for enhanced zinc-ion storage, Nano Res. 16 (2023) 503–512, https://doi.org/10.1007/s12274-022-4753-0.

[22] Y. Liu, X. Wu, Hydrogen and sodium ions co-intercalated vanadium dioxide electrode materials with enhanced zinc ion storage capacity, Nano Energy 86 (2021), 106124, https://doi.org/10.1016/j.nanoen.2021.106124.

[23] Y. Liu, Y. Zou, M. Guo, Z. Hui, L. Zhao, Boosting the active sites and kinetics of VO_2 by Mn pre-intercalated and PVP modified nanostructure to improve the cycle stability for aqueous zinc batteries, Chem. Eng. J. 433 (2022), 133528, https://doi.org/10.1016/j.cej.2021.133528.

[24] W. Zhang, Y. Xiao, C. Zuo, W. Tang, G. Liu, S. Wang, W. Cai, S. Dong, P. Luo, Adjusting the valence state of vanadium in VO_2(B) by extracting oxygen anions for high-performance aqueous zinc-ion batteries, ChemSusChem 14 (2021) 971–978, https://doi.org/10.1002/cssc.202002401.

[25] Z. Li, Y. Ren, L. Mo, C. Liu, K. Hsu, Y. Ding, X. Zhang, X. Li, L. Hu, D. Ji, G. Cao, Impacts of Oxygen Vacancies on Zinc Ion Intercalation in VO_2, ACS Nano 14 (2020) 5581–5589, https://doi.org/10.1021/acsnano.9b09963.

[26] J. Ding, Z. Du, L. Gu, B. Li, L. Wang, S. Wang, Y. Gong, S. Yang, Ultrafast Zn^{2+} intercalation and deintercalation in vanadium dioxide, Adv. Mater. 30 (26) (2018) 1800762.

[27] D. Jia, K. Zheng, M. Song, H. Tan, A. Zhang, L. Wang, L. Yue, D. Li, C. Li, J. Liu, $VO_2{\cdot}0.2H_2O$ nanocuboids anchored onto graphene sheets as the cathode material for ultrahigh capacity aqueous zinc ion batteries, Nano Res. 13 (2020) 215–224, https://doi.org/10.1007/s12274-019-2603-5.

[28] X. Dai, F. Wan, L. Zhang, H. Cao, Z. Niu, Freestanding graphene/VO_2 composite films for highly stable aqueous Zn-ion batteries with superior rate performance, Energy Storage Mater. 17 (2019) 143–150, https://doi.org/10.1016/j.ensm.2018.07.022.

[29] F. Cui, J. Zhao, D. Zhang, Y. Fang, F. Hu, K. Zhu, VO_2(B) nanobelts and reduced graphene oxides composites as cathode materials for low-cost rechargeable aqueous zinc ion batteries, Chem. Eng. J. 390 (2020), 124118, https://doi.org/10.1016/j.cej.2020.124118.

[30] P. Astuti, R.S. Rafdinal, D. Yamamoto, V. Andriamisaharimanana, H. Hamada, Hidenori Hamada Effective Use of Sacrificial Zinc Anode as a Suitable Repair Method for Severely Damaged RC Members Due to Chloride Attack, Civil Eng. 8 (7) (2022) 1535–1548.

[31] M. Slavova, E. Mihaylova-Dimitrova, E. Mladenova, B. Abrashev, B. Burdin, D. Vladikova, Zeolite Based Air Electrodes for Secondary Batteries, Emer. Sci. J. 4 (1) (2020) 18–24.

[32] J. Sun, Y. Liu, H. Jiang, X. Dong, T. Hu, C. Meng, Y. Zhang, Mn^{2+} as the "spearhead" preventing the trap of Zn^{2+} in layered Mn^{2+} inserted hydrated vanadium pentoxide enables high rate capacity, J. Colloid. Interf. Sci. 602 (2021) 14–22, https://doi.org/10.1016/j.jcis.2021.05.163.

[33] K. Zhu, W. Jiang, Z. Wang, W. Li, W. Xie, H. Yang, W. Yang, Hewettite $ZnV_6O_{16}{\cdot}8H_2O$ with Remarkably Stable Layers and Ultralarge Interlayer Spacing for High-Performance Aqueous Zn-Ion Batteries, Angew. Chem. Int. Edit. 62 (2022) e202213368.

[34] Y. Cai, R. Chua, Z. Kou, H. Ren, D. Yuan, S. Huang, S. Kumar, V. Verma, P. Amonpattaratkit, M. Srinivasan, Boosting Zn-ion storage performance of bronze-type VO_2 via Ni-mediated electronic structure engineering, ACS Appl. Mater. Interfaces 12 (2020) 36110–36118, https://doi.org/10.1021/acsami.0c09061.

[35] M. Li, J. Mou, L. Zhong, T. Liu, Y. Xu, W. Pan, J. Huang, G. Wang, M. Liu, Porous Ultrathin W-Doped VO_2 Nanosheets Enable Boosted Zn^{2+} (De)Intercalation Kinetics in VO_2 for High-Performance Aqueous Zn-Ion Batteries, ACS Sustain. Chem. Eng. 9 (2021) 14193–14201, https://doi.org/10.1021/acssuschemeng.1c04675.

[36] G. Kresse, J. Furthmüller, Efficient iterative schemes for ab initio total-energy calculations using a plane-wave basis set, Phys. Rev. B 54 (16) (1996) 11169–11186.

[37] S. Grimme, S. Ehrlich, L. Goerigk, Effect of the damping function in dispersion corrected density functional theory, J. Comput. Chem. 32 (2011) 1456–1465, https://doi.org/10.1002/jcc.21759.

[38] G. Henkelman, B.P. Uberuaga, H. Jónsson, A climbing image nudged elastic band method for finding saddle points and minimum energy paths, J. Chem. Phy. 113 (2000) 9901–9904, https://doi.org/10.1063/1.1329672.

[39] K. Momma, F. Izumi, VESTA: a three-dimensional visualization system for electronic and structural analysis, J. Appl. Crystallogr. 41 (2008) 653–658, https://doi.org/10.1107/s0021889808012016.

[40] M. Liu, M.S. Hybertsen, Q. Wu, A Physical Model for Understanding the Activation of MoS_2 Basal-Plane Sulfur Atoms for the Hydrogen Evolution Reaction, Angew. Chem. Int. Edit. 59 (2020) 14835–14841, https://doi.org/10.1002/anie.202003091.

[41] Z. Han, S. Zhao, J. Xiao, X. Zhong, J. Sheng, W. Lv, Q. Zhang, G. Zhou, H.-M. Cheng, Engineering d-p Orbital Hybridization in Single-Atom Metal-Embedded Three-Dimensional Electrodes for Li–S Batteries, Adv. Mater. 33 (2021) 2105947, https://doi.org/10.1002/adma.202105947.

[42] J. Wang, J.G. Wang, X. Qin, Y. Wang, Z. You, H. Liu, M. Shao, Superfine MnO_2 nanowires with rich defects toward boosted zinc ion storage performance, ACS Appl. Mater. Interfaces 12 (2020) 34949–34958, https://doi.org/10.1021/acsami.0c08812.

[43] S. Lian, C. Sun, W. Xu, W. Huo, Y. Luo, K. Zhao, G. Yao, W. Xu, Y. Zhang, Z. Li, K. Yu, H. Zhao, H. Cheng, J. Zhang, L. Mai, Built-in oriented electric field facilitating durable Zn-MnO_2 battery, Nano Energy 62 (2019) 79–84.

[44] L. Chen, Y. Ruan, G. Zhang, Q. Wei, Y. Jiang, T. Xiong, P. He, W. Yang, M. Yan, Q. An, L. Mai, Ultrastable and high-performance Zn/VO_2 battery based on a reversible single-phase reaction, Chem. Mater. 31 (2019) 699–706, https://doi.org/10.1021/acs.chemmater.8b03409.

[45] H. Song, Y. Liu, C. Zhang, C. Liu, G. Cao, Mo-doped LiV_3O_8 nanorod-assembled nanosheets as a high performance cathode material for lithium ion batteries, J. Mater. Chem. A. 3 (2015) 3547–3558, https://doi.org/10.1039/c4ta05616g.

[46] F. Liu, Z. Chen, G. Fang, Z. Wang, Y. Cai, B. Tang, J. Zhou, S. Liang, V_2O_5 nanospheres with mixed vanadium valences as high electrochemically active aqueous zinc-ion battery cathode, Nanomicro Lett. 11 (2019) 25, https://doi.org/10.1007/s40820-019-0256-2.

[47] W. Zhang, C. Zuo, C. Tang, W. Tang, B. Lan, X. Fu, S. Dong, P. Luo, The current developments and perspectives of V_2O_5 as cathode for rechargeable aqueous zinc-ion batteries, Energy Technol. 9 (2020) 2000789, https://doi.org/10.1002/ente.202000789.

[48] M. Chen, W. Hua, J. Xiao, J. Zhang, V.W. Lau, M. Park, G.H. Lee, S. Lee, W. Wang, J. Peng, L. Fang, L. Zhou, C.K. Chang, Y. Yamauchi, S. Chou, Y.M. Kang, Activating a multielectron reaction of NASICON-structured cathodes toward high energy density for sodium-ion batteries, J. Am. Chem. Soc. 143 (2021) 18091–18102, https://doi.org/10.1021/jacs.1c06727.

[49] G. Liu, Y. Xiao, W. Zhang, W. Tang, C. Zuo, P. Zhang, S. Dong, P. Luo, Novel aluminum vanadate as a cathode material for high-performance aqueous zinc-ion batteries, Nanotechnology 32 (31) (2021) 315405.

[50] W. Tang, B. Lan, C. Tang, Q. An, L. Chen, W. Zhang, C. Zuo, S. Dong, P. Luo, Urchin-like spinel MgV_2O_4 as a cathode material for aqueous zinc-ion batteries, ACS Sustain. Chem. Eng. 8 (2020) 3681–3688, https://doi.org/10.1021/acssuschemeng.9b06613.

[51] B. Zhang, Y. Liu, X. Wu, Y. Yang, Z. Chang, Z. Wen, Y. Wu, An aqueous rechargeable battery based on zinc anode and $Na_{0.95}MnO_2$, Chem. commun. 50 (2014) 1209–1211, https://doi.org/10.1039/c3cc48382g.

[52] M.H. Alfaruqi, V. Mathew, J. Song, S. Kim, S. Islam, D.T. Pham, J. Jo, S. Kim, J. P. Baboo, Z. Xiu, K.-S. Lee, Y.-K. Sun, J. Kim, Electrochemical zinc intercalation in lithium vanadium oxide: a high-capacity zinc-ion battery cathode, Chem. Mater. 29 (2017) 1684–1694, https://doi.org/10.1021/acs.chemmater.6b05092.

[53] G. Kasiri, R. Trócoli, A. Bani Hashemi, F. La Mantia, An electrochemical investigation of the aging of copper hexacyanoferrate during the operation in zinc-ion batteries, Electrochim. Acta. 222 (2016) 74–83, https://doi.org/10.1016/j.electacta.2016.10.155.

[54] L. Zhang, L. Chen, X. Zhou, Z. Liu, Towards high-voltage aqueous metal-ion batteries beyond 1.5 V: the zinc/zinc hexacyanoferrate system, Adv. Energy Mater. 5 (2015) 1400930, https://doi.org/10.1002/aenm.201400930.